Cement and Concrete Composites 96 (2019) 212–224

Contents lists available at ScienceDirect

Cement and Concrete Composites

journal homepage: www.elsevier.com/locate/cemconcomp

Calcium-aluminate mortars at high temperatures: Overcoming adverse conversion effects using clinker aggregates

Dimas Alan Strauss Rambo[a,b], Neven Ukrainczyk[c], Flávio de Andrade Silva[d,*], Eddie Koenders[c], Romildo Dias Toledo Filho[a], Otávio da Fonseca Martins Gomes[e,f]

[a] Civil Engineering Department, COPPE, Universidade Federal do Rio de Janeiro, P.O. Box 68506, CEP 21941-972, Rio de Janeiro, RJ, Brazil
[b] Civil Engineering Department, USJT, Universidade São Judas Tadeu, Rua Taquari, 546, 03166-000, São Paulo, SP, Brazil
[c] Institute of Construction and Building Materials, Faculty of Civil and Environmental Engineering, TU Darmstadt, Franziska-Braun-Straße 3, 64287, Darmstadt, Germany
[d] Department of Civil and Environmental Engineering, Pontifícia Universidade Católica do Rio de Janeiro (PUC-Rio), Rua Marques de São Vicente 225, 22451-900, Rio de Janeiro, RJ, Brazil
[e] Centre for Mineral Technology (CETEM), Rio de Janeiro, RJ, Brazil
[f] National Museum, Federal University of Rio de Janeiro, Av. Quinta da Boa Vista, S/N, Bairro Imperial de São Cristóvão, 20940-040, Rio de Janeiro, RJ, Brazil

ARTICLE INFO

Keywords:
High temperatures
Compressive strength
Microstructure
Calcium aluminate cement

ABSTRACT

The effect of elevated temperatures on a calcium aluminate mortar with clinker aggregates is the subject of this paper. After an exposure period of 3 h at temperatures ranging from 25 to 1000 °C, specimens were tested in residual conditions in order to evaluate changes on the mechanical and microstructural properties. A simplified hydration model based on the chemical reactions of the principal minerals is proposed to predict the evolution of matrix composition from the early-age hydration. The improvement of the mechanical properties occurring due to the conversion reactions between 25 °C and 200 °C, is attributed to an increased hydration reaction of both cement and clinker aggregate. Furthermore, when compared to the metastable reactions, an improved interlocking effect at the reactive aggregate interface, and a more dense nature of the stable hydration products, were observed. These phenomena balance the adverse effects promoted by conversion reactions on porosity and mechanical properties.

1. Introduction

Calcium Aluminate Cement (CAC) is used in various high performance applications [1–5]. In particular, the type of aggregate, and associated development of a highly porous interfacial transition zone (ITZ), has been strongly related to the degradation of concrete. In some types of high performance CAC-based concretes, calcium aluminate clinker is also used as a synthetic aggregate [5–8]. Moreover, calcium aluminate clinker, typically made by fusion of bauxite and limestone, has a high density, almost no porosity and has a polymineral grain composition that brings in a strong compatibility with CAC. This participation of aggregates in the reaction with a cementitious material creates a special “bridge effect”, which improves concrete resistance to chemical [9–13], abrasion [5,7] and thermal [6–8] attacks. In addition, CAC-based materials exhibit a rapid setting and hardening process [14,15] and can be placed in service much faster than OPC-based concretes.

In general, use of CAC-based matrices is limited to high performance applications because their high cost and well-known adverse effects on strength caused by conversion reactions. However, in certain cases the peculiar behaviour of CAC-based matrices make them economically competitive. Heerden [14] showed practical applications of CAC cements combined with reactive aggregates in fiber-reinforced shotcretes used by the mining industry in South Africa. As reported by the author, despite the high cost of CAC-based matrices, the choice for reactive aggregates (i.e.: Alag®[1] and andesite) may be the best choice in terms of cost-benefit ratio when resistance to impact, abrasion, corrosion and heat is required, as in the case of tunnel linings, where long-term durability of a well designed CAC-based lining overcomes the life time of the same structure made of OPC shotcrete. Thus, the rehabilitation costs of OPC linings make CAC-based linings definitely less expensive.

The use of reactive aggregate has been also reported by Wöhrmeyer et al. [15] which evaluated the influence of calcium aluminate aggregates on castable properties in comparison to bauxite. The obtained

* Corresponding author.
E-mail address: fsilva@puc-rio.br (F. de Andrade Silva).

[1] Alag® is a synthetic calcium aluminate aggregate (with alumina content around 40%) distributed in Brazil by Kerneos Inc.

https://doi.org/10.1016/j.cemconcomp.2018.12.002
Received 21 July 2016; Received in revised form 16 November 2018; Accepted 4 December 2018
Available online 05 December 2018
0958-9465/ © 2018 Elsevier Ltd. All rights reserved.

results indicate very little open porosity for the matrix containing calcium aluminate aggregate when compared to bauxite, even after firing at 1400 °C. Despite the lower density, the matrix produced with reactive aggregates presented higher CMOR (cold modulus of rupture) due to the better bonding (chemical affinity) between the cement paste and the aggregates.

The highly temperature-dependent hydration of CAC yields different morphologies and hydration products that continuously alter the material properties. The setting and hardening of CAC is primarily driven by the hydration of CA, whose high temperature sensitivity [1–16], yields the following main hydration products:

$$CA + 10H \rightarrow CAH_{10}\ T < 20\ ^{\circ}C \quad (1)$$

$$2\ CA + (8 + x)\ H \rightarrow C_2AH_8 + AH_x\ \text{(alumina gel)}\ T \sim 30\ ^{\circ}C \quad (2)$$

$$3\ CA + 12H \rightarrow C_3AH_6 + 2AH_3\ T > 55\ ^{\circ}C \quad (3)$$

At ambient temperatures, the metastable hydrates CAH_{10}, C_2AH_8 and AH_x convert to more stable C_3AH_6 and AH_3 (eqs. (4)–(6)) with the release of water and consequent impairment of the material porosity, permeability and mechanical properties. The conversion is accelerated by temperature increase and moisture availability enhancing the dissolution and re-precipitation processes to take place.

$$3CAH_{10} \rightarrow C_3AH_6 + 2AH_3 + 18H \quad (4)$$

$$3C_2AH_8 \rightarrow 2C_3AH_6 + AH_3 + 9H \quad (5)$$

$$AH_x\ \text{(alumina gel)} \rightarrow \text{(Gamma) - } AH_3\ \text{(gibbsite)} + (x\text{-}3)H \quad (6)$$

This adverse conversion effect has to be taken into account, as it may cause a significant strength reduction, which is why using CAC-based concretes is forbidden for structural applications in some countries. Earlier construction failures in the history of CAC-based concretes show that the design should be based on the final properties (after conversion), primarily strength, and the water/cement mass ratio (w/c) should not exceed 0.4 and checks are needed in the building site. New generations of superplasticisers offer novel possibilities to improve workability and lower the w/c ratio as well [17], which could aid the long-term performance of CAC-based materials. However, it is well known that in CAC mortars, with conventional (non-reactive) aggregates, the converted material always shows a low compressive strength, owing to the conversion process. The most interesting finding reported in the present paper is the improvement of the mechanical properties with ongoing conversion reactions, which occur in both conditions, i.e. when the mortar is cured at room temperature or it is exposed to 200 °C. Overruling the adverse conversion effects depends on the use of both Alag aggregates and a low w/c ratio.

Conventional cement-rich castables [18] are used in high-temperature applications up to about 1000 °C [1]. They exhibit a characteristic drop in strength at intermediate temperatures due to the conversion hydration reactions as well as slow sintering which does not allow for the development of ceramic bonds after breaking down the hydraulic bonds. Sufficient cement content is essential to maintain an adequate minimum strength at 1000 °C; above that temperature stronger ceramic bonds result again in an increase in strength. The phases crystalized at high temperatures depend markedly on the composition of CAC and aggregates. The high lime content of conventional castables favors the formation of low melting phases like mayenite ($C_{12}A_7$ and CA), which are known to degrade the refractoriness at higher temperatures (above 1000 °C). Advanced refractories, for applications above 1100 °C, are made with low and ultra-low cement contents (with the overall CaO content less than 2.5%), containing micron-sized mineral additives [16,19]. These types of refractories, are the object of extensive research efforts, but are out of scope of the current paper. Aggregates used in CAC refractory castables include a dense packing of fused alumina, chromite, sintered bauxite, chamotte and exfoliated vermiculite [1,6–8].

Studies in the field of CAC-based refractory castables with clinker aggregates are scarce and of little use. Therefore, this paper investigates the effect of elevated temperatures on microstructural properties, synergetic ITZ bond, and resulting mechanical strength evolution of CAC mortar with clinker aggregates. The compressive strength of CAC mortar was measured in two different conditions, i.e. when the specimens were cured at room temperature (7, 14 and 28 days) and exposed to elevated temperatures (from 25 to 1000 °C). The transformation hydration reactions and dehydration process of the mortar were investigated using TGA, SEM, XRD and porosimetry analysis. A simple hydration model based on the main chemical reaction scheme of the principal minerals was employed to predict the evolution of the cement-paste composition during early age hydration at room temperature, and the transformation and dehydration reactions of CAC at higher temperatures. The model was used to predict the evolution of solid-volume fraction, porosity, chemical bond and water release (due to evaporation). In order to compare the predictions yielded by the paste model with the experimental results obtained at mortar level, the predictions were normalized to the mass or volume of the cement paste component. To this purpose, the mortar was represented as a homogenous mixture of air bubbles, aggregates and evolving cement paste microstructure. In this case, the paste consisted of hydration products (formed by reacting cement and water) and internal porosity resulting from chemical shrinkage [20].

2. Materials and methods

2.1. CAC mortar

The materials employed in the CAC mortar composition were commercially-available calcium aluminate cement (Secar 51 from Kerneos Inc.) and synthetic calcium aluminate aggregate (Alag from Kerneos Inc.), polycarboxilate superplasticizer in powder (Peramin CONPAC 500 from Kerneos Inc.) and methyl-cellulose as viscosity modifier agent to avoid segregation. Oxide composition of the CAC and aggregates as obtained by XRF (EDX 720, Shimadzu Co. with rhodium tube and Silicon detector) is given in Table 1. The mineralogical composition of the CAC and Alag obtained by QXRD (section 2.4.1) is: 60% CA, 22% C_2AS, 4% $C_{12}A_7$ with CT, ferro perovskite and pleocroite as remaining phases, and 45% CA, 16% C_2AS, 11% $C_{12}A_7$ with $C_2A_xF_{1-x}$, C_2S, respectively. Alag has particle diameters ranging from 0.001 mm to 1.18 mm. The water/cement mass ratio of the refractory concrete was 0.35. Fig. 1 shows the grain size distribution of the used cement and aggregate determined by mechanical sieving [21] (diameter >

Table 1
Chemical composition of the calcium aluminate cement and of the synthetic calcium aluminate aggregate.

Cement		Aggregate	
Compound	Content/%	Compound	Content/%
Al_2O_3	51.45	Al_2O_3	39.88
CaO	38.51	CaO	36.02
SiO_2	3.07	SiO_2	2.79
Fe_2O_3	1.76	Fe_2O_3	14.48
TiO_2	1.89	TiO_2	1.61
SO_3	0.61	SO_3	1.05
K_2O	0.42	K_2O	0.19
ZrO_2	0.12	ZrO_2	0.09
MnO	0.02	MnO	0.19
SrO	0.05	SrO	0.03
Ga_2O_3	0.01	Ga_2O_3	0.15
Y_2O_3	0.01	Y_2O_3	0.01
Ta_2O_5	0.03	P_2O_5	1.77
Cr_2O_3	0.07	V_2O_5	0.06
NbO	0.01	LOI	1.68
LOI	1.96		

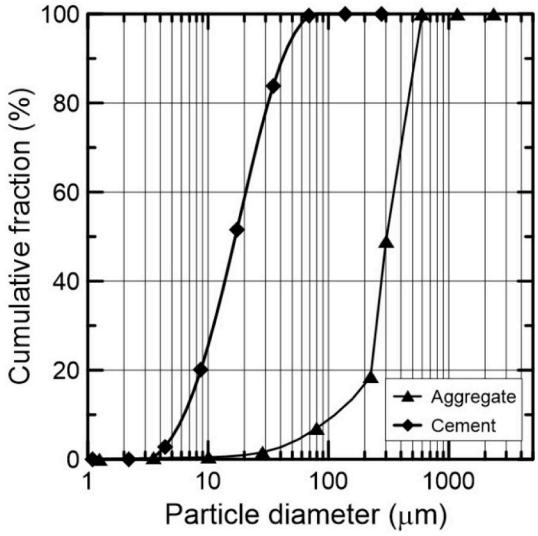

Fig. 1. Particle size distribution of the used aluminous cement and aggregate.

Table 2
Mix composition.

Composition	
Synthetic calcium aluminate aggregate (kg/m^3)	1264.4
Calcium Aluminate Cement (kg/m^3)	670
Powder polycarboxilate superplasticizer (kg/m^3)	4.35
Viscosity modifier agent - VMA (kg/m^3)	0.502
Water (kg/m^3)	234.5
Superplasticizer content (%)	0.65
Water/cementitious mass ratio	0.35

300 μm) and laser granulometry (diameter < 300 μm). Table 2 gives the composition of the concrete matrix. To achieve elevated compressive strength values, the CAC mortar used in this research was designed following the compressible packing model (CPM) routine [22,23]. The model was optimized for experimental compactness, size grading distributions and specific gravity of the constituents (cement and synthetic aggregate) as well as for the saturation dosage of the chemical additive that was in the form of a powder.

2.2. Heating and drying regime

Cylindrical specimens measuring 50 × 100 mm (diameter x height) were cured for 7, 14 and 28 days at 25 °C in sealed conditions (without water exchange with environment) for later use in physical and mechanical tests. The heating rate, the target temperatures and the sequence of steps adopted for the present study can be found in the scheme found in Fig. 2. The specimens cured for 7 days (established as a reference age for the mechanical tests) were then heated up to 200, 400, and 1000 °C (three specimens for each temperature) and subsequently cooled by a natural process inside the furnace. An electric furnace with radiant heating (metal alloy type Kanthal "A1" in alumina tubes) internally protected by perforated ceramic plates was used. The heating rate was set to 10 °C/min. The temperature level was kept constant for 1 h at each targeted temperature. The furnace was cooled down before the specimens were removed in order to avoid thermal shock. The rate of cooling was not controlled but followed a natural quasi-steady thermal process.

Experiments on specimens stored at room temperature, without additional heating, were also carried out. Drying of these specimens (labeled 25 °C) was achieved by using a vacuum pump for 30 days. Drying of specimens by heating was not done because of the effect of the transformation reactions [1] that significantly modifies the pore microstructure of CAC-based materials.

Release of water (*RW*, in vol% of the mortar) due to exposure of the specimens to high temperatures (200, 400 and 1000 °C) or vacuum drying at 25 °C is obtained from weight measurements before exposure to heat (W_{before}), the dry weight after exposure (W_{after}), and the sample volume (obtained by Archimedes method) W_{Arch}, according to the following equation:

$$RW = \frac{W_{before} - W_{after}}{W_{Arch}} \times 100 \quad (7)$$

2.3. Compressive strength test

Compression tests were performed in a Shimadzu universal testing machine model UH-F1000 kN with a computer-controlled hydraulic servo system. Three cylindrical specimens measuring 50 mm × 100 mm (diameter x height) were tested for each of the curing periods (7, 14 and 28 days at 25 °C). The tests were carried out at a rate of 0.1 mm/min. Before testing, the cylinder faces were smoothed at the lathe. The axial strain of the cylinders was measured using two LVDT's attached to the sample by steel rings (gage length of 50 mm).

2.4. Microstructural characterization

The mortar matrix was investigated using a scanning electron microscope (SEM) FEI Quanta 400. For this, matrix samples (tested under compression) were cut from specimens, with dimensions of 20 × 20 mm (length x width). The samples were coated with a 20 nm gold layer to become conductive and suitable for conventional SEM analysis. The SEM was operated using 25 kV of accelerated tension and 30 mm of working distance.

TGA analyses were carried out using the powder obtained from crushed fragments of the specimens tested under compressive loading. The thermal analyses were performed in a TA Instruments, SDT Q600 model TGA/DTA/DSC simultaneous apparatus with temperatures ranging between 35 and 1000 °C using 100 mL/min of nitrogen flow, using platinum sample holders. In order to eliminate the residual unbonded water, an isothermal step at 35 °C for 1 h was applied before commencing the analyses. Bound water in the dried specimens was obtained from a mass loss between 35 and 550 °C and related to the mass of the anhydrous solid mortar material obtained after firing at 1000 °C.

2.4.1. Powder X-ray diffraction

The composition of CAC cement, Alag aggregates and mortars were investigated by powder X-ray diffraction (XRD). Operating conditions for qualitative analysis of the Bruker D8 advance instrument were set to 40 kV and 40 mA using CuK$\alpha_{1,2}$ radiation 2θ value between 3 and 55°. For quantitative analysis, operating conditions of the Bruker-AXS D4 ENDEAVOR diffractometer were set to 40 kV and 40 mA, using Fe-filtered CoK$\alpha_{1,2}$ radiation (λ_1 = 0.1789 nm, λ_2 = 0.1793 nm). Cobalt radiation was selected over copper in order to minimize micro-absorption, i.e. in general larger absorptions of CuKα radiation by iron (oxides) in the sample [24] and fluorescent background as well as better angular dispersion of the diffraction lines due to longer wave length. Diffractograms were recorded from 4° to 105° 2θ, in 0.02° 2θ increments. A LYNXEYE linear Si-strip-type detector was used with an opening of 3.8° 2θ, being equivalent to 188 active channels. A counting time of 1.85 s per increment and channel was used, resulting in a total measurement time per scan of about 2.6 h. Only qualitative diffractograms (with standard CuK$\alpha_{1,2}$ radiation) are shown here. In order to enable a qualitative and quantitative analysis, samples were prepared using crushed mortar material. For quantitative analysis ten percent of corundum in mass was added as internal standard to samples (> 3 g for mortars) and then further grounded to enhance the number of particles analysed, to improve powder homogeneity and packing characteristics, and to minimize micro-absorption related problems. Corundum was a

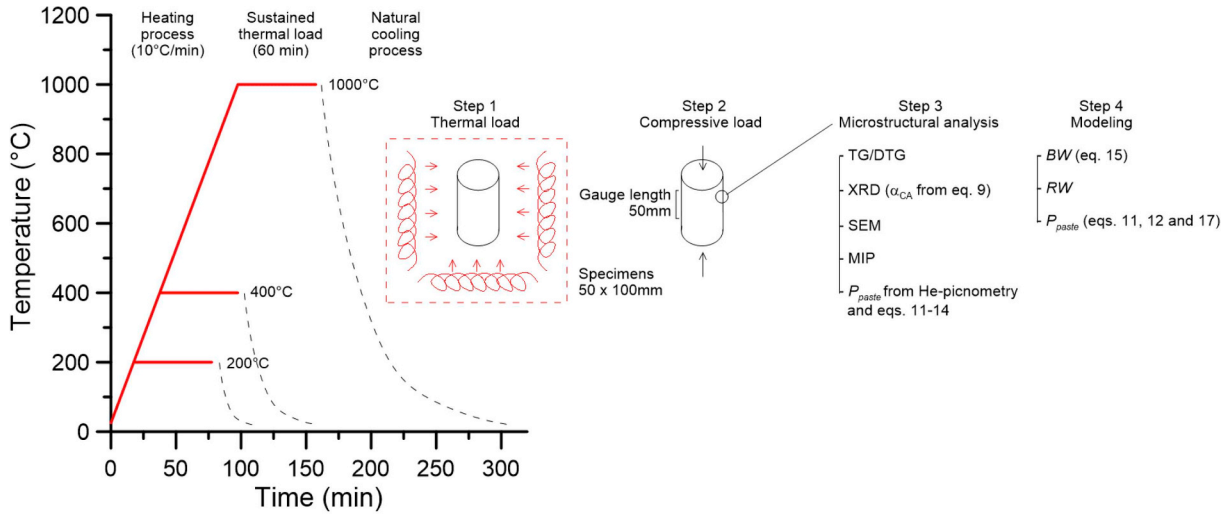

Fig. 2a. Schematic diagram of the heating ramp, target temperatures and the sequence of steps adopted for the present study. Degree of reacted CA was obtained from XRD measurements and eq. (9) and was used as input for modeling predictions. Modeling outputs are: *BW*-bound water (eq. (15)), *RW*-released water (a difference between the total 'mixed' water and *BW*), and *P*-porosity (eqs. (11), (12) and (17)).

reasonable choice as it was assured by preliminary qualitative XRD analyse that no traces of corundum were detected in original samples (detailed further in the Discussion section). Quantitative XRD analysis of specimens was done using the adiabatic principle with auto flushing [25] as a proven method [26]. Here, the matrix-flushing method was applied as it enables to directly quantify relative mineral portions in samples including both the crystalline and amorphous components by analyzing for only those components of interest. Here only CA and $C_{12}A_7$ (and C_2AS only in CAC cement and Alag as raw materials but not in hydrated mortar specimens), while quantification of other minerals (e.g. pleochroite, C_2S, FeO, CT, ferro perovskite and $C_2A_xF_{1-x}$) and amorphous phases were and can be omitted. The criterion for this method is that the reference material (here corundum) should have close level of crystallinity, i.e. very similar level of perfection or imperfection in a crystal structure, as the quantified component in the sample. The Full-Width at Half- Maximum of reflections in an X-ray diffraction pattern was compared as an indication of the crystallinity of the components, showing no significant differences. It is important to note that the possible effect of the difference in crystallinity is lowered by using peak areas instead of peak heights to define and quantify the diffraction peak intensity. In the matrix-flushing method the relationship between intensity (peak area) of the characteristic X-ray reflection I_m is directly proportional to the weight fraction of the component by a factor k_m which contains the mass absorption coefficient of the total sample. The k_m values were determined by mixing the pure phase, whose syntheses is described in Ref. [27], with standard corundum in a 50:50 wt ratio. Appropriate corrections for peak overlaps were meticulously applied by inference to diffraction peak areas of the pattern due to pure synthetic phases. Mass fraction of mineral w_{m_XRD} in XRD sample is calculated according to:

$$w_{m\_XRD} = k_m \, w_A \, I_m / I_A \tag{8}$$

It is difficult to separate CA reactivity coming from cement or from the Alag aggregates. Therefore, a new procedure was developed to

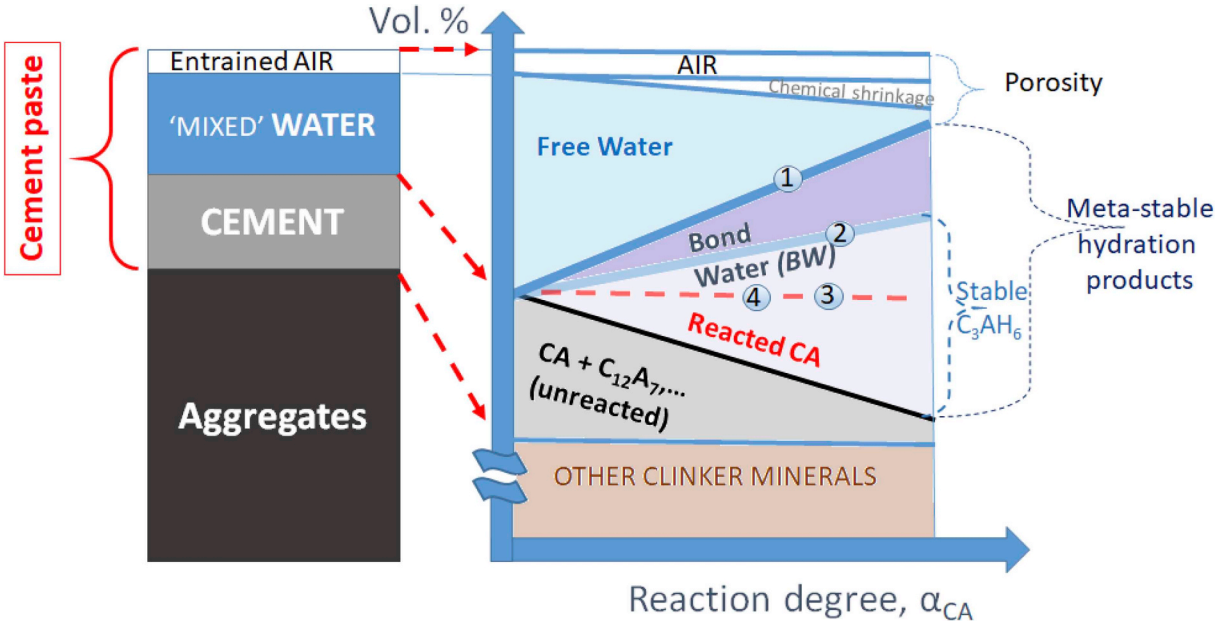

Fig. 2b. Scheme of the modeling approach (arbitrary scale). Points 1 to 4 in the graph represent curing scenarios: 25 °C (1), 200 °C (2), 400 °C and 1000 °C (4). Modeling values are compared with experimental results in Figs. 10 and 11.

enable this analysis where Alag reactivity is considered as an additional 'virtual' reactivity of cement. Such a degree of reacted CA is obtained by normalizing it to the initial amount of CA in cement which is then easily calculated according to:

$$\alpha_{CA} = (w_{CA,0} - w_{CA,t})/w_{CA,0} \quad (9)$$

where $w_{CA,0}$ is the initial mass fraction of CA in anhydrous CAC (i.e. before hydration) and $w_{CA,t}$ represents the mass fraction of CA after hydration reactions, also normalized to the mass of anhydrous CAC, which is calculated as:

$$w_{CA,t} = w_{CA\_XRD}\,(1 + BW\,M_{cem}) - M_{Alag}\,w_{CA\_Alag} \quad (10)$$

where w_{CA_XRD} is the mass fraction of CA in the sample undergone XRD analysis that comprises cement, Alag aggregates and chemically bound water, BW expressed in g/g of cement; M_{cem} is the mass fraction of cement in anhydrous mortar (0.346, Table 2), M_{Alag} is the mass fraction of Alag aggregates in anhydrous mortar (0.654) and w_{CA_Alag} is the initial amount of CA in Alag. The degree of reacted CA obtained by eq. (9) can thus have values greater than 1, meaning that all CA from cement is consumed, but also an additional CA from Alag has reacted. In other words, the results were normalized to cement, but the overall CA coming from both cement and Alag is considered in eqs (9) and (10).

2.4.2. Porosimetry

Mercury intrusion porosimetry (MIP) measurements were carried out with Pascal 440 from Thermo-Scientific, in accordance with the procedure described in the ISO 15901-1/2005 standard. The volume of mercury, which penetrates the sample, is a function of the applied hydrostatic pressure (up to 400 MPa). The pore diameter was calculated with the Washburn equation. Mercury properties are: density 13.53 g/cm^3, surface tension 0.485 N/m, and contact angle 130°. The measurements were performed with gradual reading for each applied pressure (increase speed of about 10 MPa/min), on the previously dried sample with an evacuation pressure of 50 μm Hg during 5 min.

Apparent density and air content of mortars were determined following ASTM C185-08 (2008). The volume and mass of the hardened mortar specimens, cured in sealed conditions, was measured as well. The air content (14%) is calculated from the measured apparent density of the mortar specimens, from the known densities of the constituents (Table 2), and the mixture proportions.

Density of the powdered mortar specimens was measured using Pycnomatic ATC (Thermo-Scientific) instrument with Helium as a working gas medium. Based on this density, a new procedure is presented here to calculate the theoretical porosity of cement paste:

$$P_{paste} = 1 - \frac{v_{soild}}{v_{paste}} \quad (11)$$

where v_{solid} is the volume of cement paste solids comprising of the remaining cement and formed hydration products (Fig. 2b), and v_{paste} is the volume of cement paste which adds also the remaining unreacted capillary water but without considering the volume of air bubbles. Normalizing these volumes to 1 g of cement, they are calculated as:

$$v_{paste} = \frac{1}{\rho_{cem}} + \frac{w/c}{\rho_{H_20}} \quad (12)$$

$$v_{solid} = \frac{1 + BW}{\rho_{solid}} \quad (13)$$

where w/c is the water to cement mass ratio (0.35), BW is chemically bond water in g/g of cement, ρ_{cem} and ρ_{H2O} are the densities of cement and water, respectively, and ρ_{solid} is the density of the solids in the paste, which can be measured when working with pastes (without aggregates), but here for mortars it is obtained by combining eq (13) with following equation (14) for the theoretical density of the mortar:

$$\rho_{mort,\,s} = \frac{1 + BW + m_{alag}}{v_{solid} + \frac{m_{alag}}{\rho_{alag}}} \quad (14)$$

where $\rho_{mort,s}$ is the measured density of the solids in the mortar, m_{Alag} is mass of Alag per 1 g of cement (=1265/750, from Table 2) and ρ_{Alag} is density of Alag. The solid paste volume, v_{solid} can be calculated by extracting from eq. (14) where it is the only unknown value.

2.5. Modeling

Modeling CAC hydration requires knowledge on the stoichiometry and kinetics of the hydration reactions. This information is not yet fully available due to the complexity of the commercial cement hydration process. As a first approximation, however, only principal (congruent) hydration reactions in their pure form can be considered. In the case of both iron-rich (Alag) aggregates and low-iron (Secar 51) cement, most hydraulic phases are CA and $C_{12}A_7$, while the rest of the phases (C_2S, C_2AS, C_4AF, perovskite and pleocroite) may be considered to have no significant reactivity (especially at low w/c ratios and sealed curing conditions). The main effects of $C_{12}A_7$ are on the dissolution rate, which is accelerated, and on the occurrence of a small quantity of C_2AH_8 even at low temperature hydration when eq. (1) is dominant. Moreover, $C_{12}A_7$ is present in much smaller quantities (generally 2–7%) than CA (40–70%) and gives similar products as CA hydration, predominantly CAH_{10} and C_2AH_8 (which transform at elevated temperatures) [1,28]. The evolution of chemically bound water (BW) during hydration can be expressed as:

$$BW = \sum_m (\mathrm{H}/m)_{tot}\,w_m\,\alpha_m \quad (15)$$

where the sum is done over all reactive minerals m, in order to generalize the model, but in this paper only equations (2) and (3) for CA are considered, α_m is the degree of reaction for mineral m, w is the mass fraction of mineral in cement, and

$$(\mathrm{H}/m)_{tot} = \frac{M_{\mathrm{H}}\,\upsilon_{\mathrm{H}}}{M_m\,\upsilon_m} \quad (16)$$

$(\mathrm{H}/m)_{tot}$ is the stoichiometric water-to-cement ratio for complete hydration of mineral m calculated from molar masses M, and stoichiometric coefficients in the reaction scheme υ. For the case when all $\alpha_m = 1$ the value for BW corresponds to the stoichiometric water requirement in g per g of CAC.

During setting and hardening, the microstructure of material and amounts of certain phases are changing. During hydration, both volume fractions of the non-reacted cement and free water decrease, while the fractions of formed hydration products increase. The solid fraction comprises the formed hydration products and fraction of non-reacted cement (Fig. 2b). The paste solid volume content (in cm^3/g CAC) can be formulated as:

$$v_{soild} = v_{CAC,0} + \sum_m (v_{hydrates} - v_{m,o})w_m\alpha_m \quad (17)$$

Where $v_{CAC,0}$ and $v_{m,0}$ is the initial (non-hydrated) specific volume of cement ($v_{CAC,0}$ is in cm^3/g) and mineral m ($v_{CA,0}$ in cm^3/g of CA mineral), respectively, and $v_{hydrates}$ is the volume of formed hydration products per 1 g of completely reacted mineral m (in first approx. only CA) calculated as:

$$v_{\mathrm{hydrates}} = \sum_h \left(\frac{M_h\,\upsilon_h}{M_{\mathrm{m}}\,\upsilon_{\mathrm{m}}\,\rho_h} \right)_{\mathrm{hydrates}} \quad (18)$$

Volume fractions are obtained by normalizing/dividing eq. (17) with the volume of cement paste (v_{paste}, eq. (12)) containing 1 g of cement. In eq. (18) the sum is over all hydration products (e.g. $h = C_2AH_8 + AH_3$ for reaction eq. (2)), υ_h and M are the stoichiometric coefficient and molar masses of the reaction components, respectively,

Table 3
Densities [29,30] and molar masses of the hydration reactants and products, used for modeling porosity.

Component	ρ/g cm^{-3}	M/g mol^{-1}
CA	2.98	158.1
$C_{12}A_7$	2.85	138.7
CAH_{10}	1.72	338.1
C_2AH_8	1.96	358.2
C_3AH_6	2.52	378.3
AH_3	2.44	156.0

and ρ_h is the density of a hydration product [29,30] (Table 3). Note that for reaction (2) AH_x is approximated as AH_3 gibbsite, because it is difficult to separate reactions eqs. (2), (5) and (6), and furthermore C_2AH_8 and AH_x are sensitive to drying due to releases of their loosely-bond water (up to C_2AH_5 [31]).

Depending on the water to cement mass ratio, H/CAC and initial amount of reactive minerals in CAC the reaction of hydration can be stopped by insufficiencies of 'free' water or by a ceasing of the reactive cement minerals. Another possibility to terminate hydration, in the case of water saturated conditions, is an insufficient free space for the growth of reaction products. Thus, the model eqs. (15) and (17) are valid for:

$$0 \leq BW \leq (\mathrm{H/CA})_{\mathrm{tot}} \tag{19}$$

and for

$$v_{\mathrm{CAC},0} \leq v_{\mathrm{solid}} \leq v_{\mathrm{paste}} \tag{20}$$

Note that in eq. (20) the right hand side is the volume of cement paste (eq. (12)) which is considered here not to change during hydration. The model of cement-paste porosity presented in this paper does not contain entrained air bubbles. Upscaling of the paste model to the mortar level, is based on a simple volume balance homogenization, where a mortar is represented as a homogenous mixture of air bubbles, aggregates and cement paste (Fig. 2b). Due to calibration/validation and experimental difficulties, the individual reactivity of aggregate and cement was not considered separately. The effect of aggregate reactivity was simplified via an additional virtual increase in the degree of cement reaction.

3. Results

3.1. Mechanical tests

3.1.1. Influence of age on compressive strength of CAC mortar

Fig. 3 shows representative stress–strain curves obtained from compression tests (at room temperature) performed with the CAC mortar at an age of 7, 14 and 28 days. All specimens showed a brittle behavior under compression load since the first micro-cracks propagate throughout the specimens creating an interconnected network of micro-cracks which turn to large macro-cracks up to failure. As expected, the average stress levels achieved by specimens at the target ages were very close, given the short setting time and high mechanical strength of the CAC mortar. With respect to the ultimate compressive strength (σ_{UCS}), enhanced curing times to 14 and 28 days showed increases of, respectively, 7% and 12% in comparison to the CAC matrix with 7 days of age. Table 4 provides the corresponding values. This continuous increase in strength up to 28 days (at 25 °C) is contrary to the well-known conversion process during CAC hydration which decreases the mechanical properties of conventional CAC-based materials. Main reason for this new finding is related to the incorporation of reactive Alag aggregates and a low w/c ratio, which will be discussed later in this paper. Since at 7 days of age the CAC mortar reached 90% of the 28 days compressive strength, this period (7 days) was established as a reference for the mechanical tests performed to study the temperature effect.

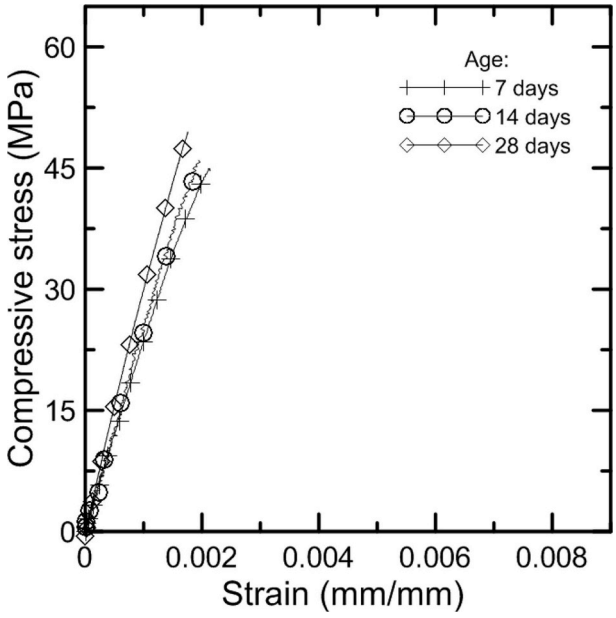

Fig. 3. Compressive strength - strain curves of CAC mortar at 7, 14 and 28 days of age.

Table 4
Mechanical properties for different ages.

Age (days)	First crack values			
	P_{UCS} (kN)	σ_{UCS} (MPa)	ε (mm/mm)	E_C (GPa)
7	89.78 (6.55)	45.72 (3.33)	0.00217 (0.000195)	25.05 (1.09)
14	96.19 (12.62)	48.98 (6.43)	0.00212 (0.000223)	23.25 (4.17)
28	100.80 (3.42)	51.34 (1.74)	0.00177 (0.000067)	31.25 (1.25)

3.1.2. Effect of temperature on compressive strength of CAC mortar

The evolution of the mechanical strength of CAC mortar submitted to elevated temperatures is presented in Fig. 4. Results obtained from the specimens are given in Table 5. The CAC mortar showed to be strongly affected by thermal impact when submitted to a compressive loading. When preheated up to 200 °C the CAC mortar showed a substantial increase in compressive strength of 24%. From this temperature and above, the compressive strength values decreased gradually with increasing temperature. In comparison with the results obtained at room temperature, the decreases in compressive strength for 400 °C and 1000 °C were, respectively, 22% and 57%. Similar trend as observed for the compressive strength was reflected by the elastic modulus (see Fig. 4). When preheated up to 200 °C, the CAC mortar showed a slight increase in the elastic modulus of 8%. At temperatures between 200 °C and 1000 °C, severe loss was observed in the elastic modulus. In comparison with CAC mortar tested at room temperature, the decreases in elastic modulus (E_C) for mortars heated at 400 °C and 1000 °C were 58% and 70%, respectively. As well as the influence of age, the effect of temperature will be further addressed in the discussion section, where mechanical results are correlated with the physical and chemical changes occurring in the microstructure of CAC mortar.

3.2. Microstructural analysis

The TG curves are plotted starting from the end of the aforementioned isothermal stage at 35 °C (Fig. 5). The DTG peaks presented by the unheated sample (25 °C), comprehended between 35 and 200 °C, are related to different process which include: loss of free and loosely

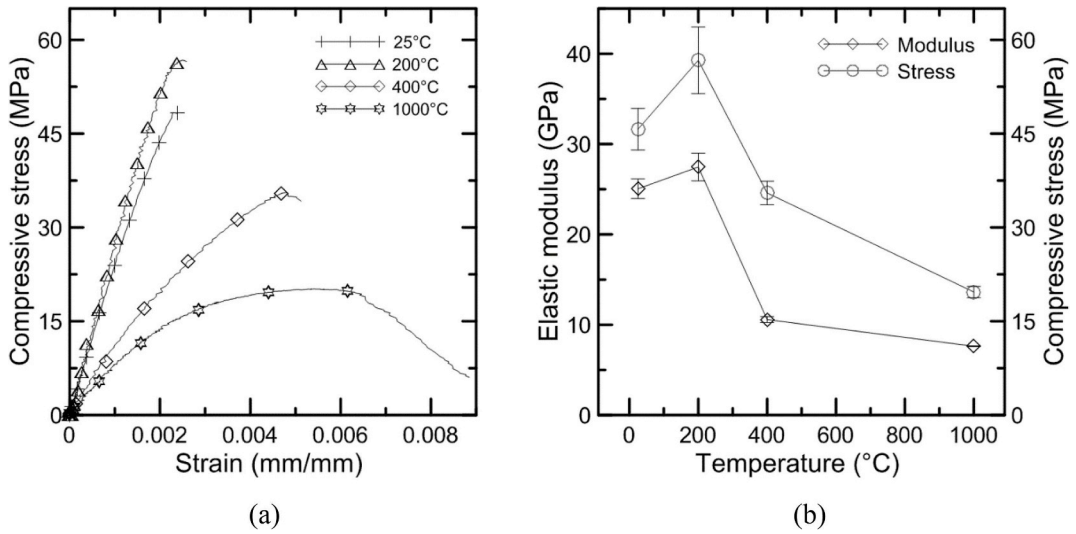

Fig. 4. Effect of temperature on the residual compressive strength (a) and elastic modulus (b) of CAC mortar (7 days of age).

Table 5
Effect of temperature on mechanical properties (7 days of age).

Temperature	Values			
	P_{UCS} (kN)	σ_{UCS} (MPa)	ε (mm/mm)	E_C (GPa)
25 °C	89.78 (6.55)	45.72 (3.33)	0.00217 (0.00019)	25.05 (1.09)
200 °C	111.36 (10.42)	56.72 (5.31)	0.00234 (0.00033)	27.46 (1.53)
400 °C	69.72 (3.66)	35.51 (1.87)	0.00481 (0.00029)	10.57 (0.34)
1000 °C	38.63 (1.77)	19.67 (0.90)	0.00537 (0.00011)	7.62 (0.41)

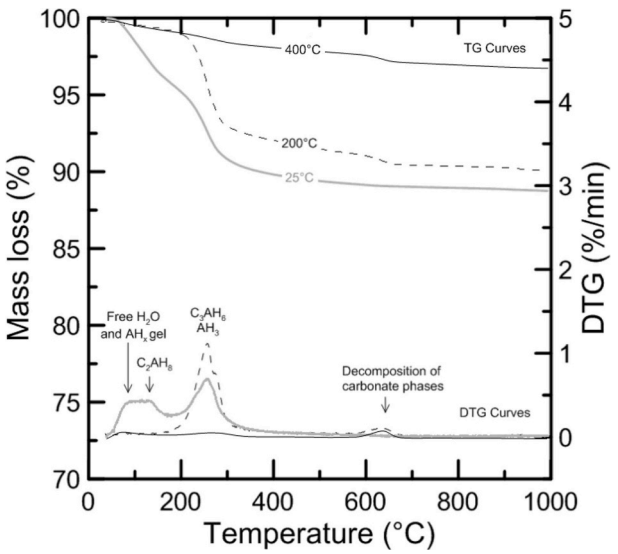

Fig. 5. Thermal analysis of CAC mortar at 7 days of age and after exposure to 200 and 400 °C.

held structural water of the AH_x gel and dehydration of the metastable C_2AH_8 [14]. As shown in Fig. 6 the crystalline structure of metastable hydrate C_2AH_8 was also detected by XRD. The same DTG peaks (between 35 and 200 °C) are not visible in the other curves given the heating process applied to both (200 and 400 °C) specimens. Between 200 and ~350 °C, both the unheated sample (25 °C) and samples heated up to 200 °C, presented significant mass losses. These losses correspond primarily [14] to dehydration of the stable phases C_3AH_6 and AH_3, which persist after heating and drying of the CAC mortar. These phases are also detected by XRD (see Fig. 6). Since main hydration products presented by the CAC matrix decompose under temperatures below 400 °C, the samples 400 and 1000 °C did not show significant mass losses. This mass loss can be attributed to some remaining crystalline water in $C_{12}A_7H$ [32] and AlOOH [33,34], but also to a decomposition of the carbonate phases after about 600 °C, as heating of the specimens could be accompanied by some degree of carbonation. No traces of C_2ASH_8 were observed by XRD, indicating low reactivity of C_2AS, probably due to low w/c ratio and sealed curing conditions.

XRD analysis on specimens obtained from hydrated specimens cured at different conditions, shown in Fig. 6, confirmed the hydrate compositions expected from literature [1,12]. The main hydration products observed on 25 °C samples was C_2AH_8 with traces of AH_3 and C_3AH_6. The sample heated up to 200 °C presented a substantial increase in diffraction peaks for C_3AH_6 and AH_3, accompanied by a decrease in diffraction peaks for CA. This process is related to a conversion process accompanied by further hydration of reactive CA minerals. Diffraction peaks of metastable hydration products and aluminium hydroxide are fairly broadened, indicating poor crystallinity, while that of C_3AH_6 showed a good crystallinity.

At 400 °C XRD results show traces of amorphous diffraction peaks for C_3AH_6 and an increase in the amount of $C_{12}A_7$ accompanied by loss of its crystallinity as observed by its peak widening. At 1000 °C XRD reveals an increase in the level of $C_{12}A_7$ crystallinity and a strong increase in CA diffraction lines, demonstrating crystallization of CA and $C_{12}A_7$. The amount of reacted and re-crystalized CA and $C_{12}A_7$ phases as a function of temperature is quantified from XRD measurements (in discussion section).

Further experimental results performed on CAC mortar specimens and samples are presented in Table 6. Release of water (*RW*) due to the drying effect, expressed in vol. % of mortar specimen, indicates an increased evaporation of 'free' water from the specimens, with increasing exposure temperature. At 25 °C upon vacuum drying, mass loss of the samples is due to evaporation of 'free' water but also because of the loosely held structural water in C_2AH_8 (- > C_2AH_5 [14]) and AH_x metastable hydration products. At 200 °C the specimen loses 145% more water than during vacuuming at the 25 °C specimen. This increase can be attributed to conversion reactions which occur under hydrothermal conditions within the specimen, i.e. combined high temperature and water availability due to a low vapor diffusion process through the material. Such a conversion reaction results in a production of more 'free' water (eqs. (4)–(6)). Eventually, at time of exposure in the furnace, this free water could be evaporated from the specimen. At 400 °C, the amount of water release is 136% higher than at 200 °C, due to decomposition of stable hydration products. At 1000 °C, the specimen

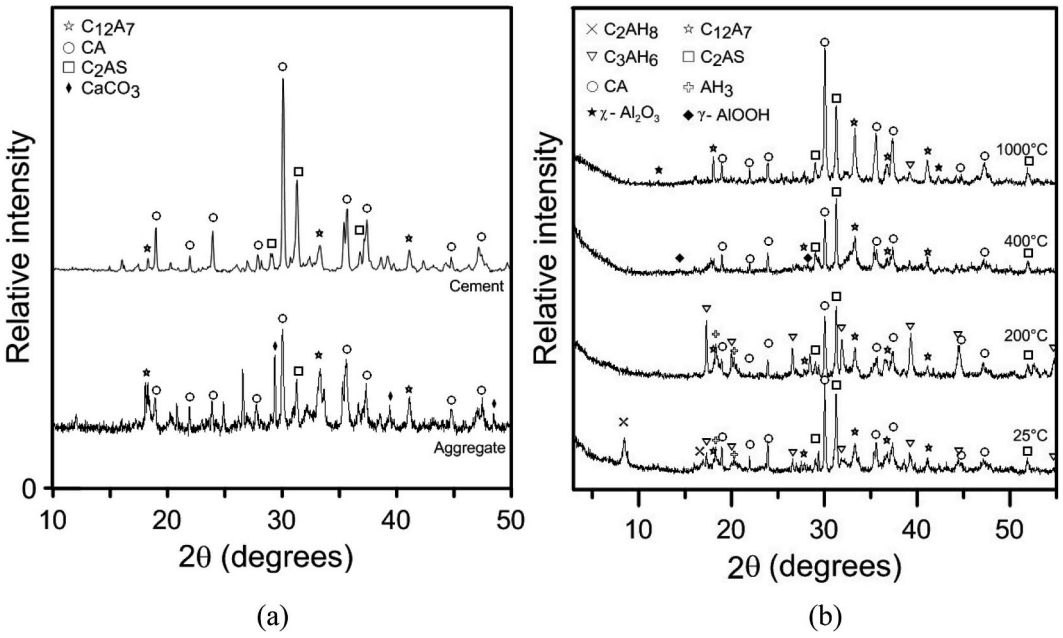

Fig. 6. XRD profiles for cement and aggregate (a) and for CAC mortar at room temperature and preheated at 200, 400 and 1000 °C (b).

Table 6
Experimental results performed on CAC mortars: release of water due to high temperatures (200, 400 and 1000 °C) or vacuum drying at 25 °C (in vol. % of mortar); chemically bonded water remained after high temperature or vacuum treatment (in g/g of anhydrous solids, i.e. normalized to the mass of fired mortar which comprises cement and aggregate); density of mortar solids, i.e. skeleton density g/cm^3, measured on grinded samples; MIP porosity (in vol. % of mortar).

Specimen	Water release (*RW*), vol. % mortar	Bound water (*BW*), g/g dry solids	Mortar solids density, g/cm^3	MIP porosity, vol. % mortar
25 °C[a]	3.6	0.1044	2.799	21.9
200 °C	8.9	0.0780	2.906	26.1
400 °C	20.9	0.0283	3.034	33.5
1000 °C	26.3	0.0023	3.172	38.8

[a] Vacuum dried.

exhibits 25% higher water release than at 400 °C due to a more complete decomposition of hydration products, as well as carbonates formed by the carbonation process during the heating regime.

Chemically bonded water that remained inside the specimens, was obtained from TG measurements and expressed in g/g of anhydrous solids, i.e. normalized to mass of fired mortar solids (at 1000 °C) which comprises anhydrous cement and aggregate. As expected from the conversion reactions (eqs. (4)–(6)), the results show a decrease in bonded water (*BW*), and an increase in mercury intrusion porosity (MIP), with enhancing temperature. Mortar solids density, measured on powdered specimens, increases with temperature in agreement with a simultaneous decrease of the chemically bonded water.

Effect of temperature on the cumulative pore size distribution (MIP, Fig. 7) shows a coarsening of the pore sizes at 400 and 1000 °C. However, interestingly, metastable samples at 25 °C exhibits a coarser pore size distribution than the converted sample at 200 °C. This could be attributed to the sensitivity of a loosely held structural water in C_2AH_8 and AH_x gel to drying [14] (Figs. 8 and 9), but could indicate a possible change in pore morphology due to a re-distribution of hydration products within the pore space during conversion reactions as well. Unfortunately it is difficult to separate these two effects.

Specimens cured at 25 °C, formed plate-shaped C_2AH_8 crystals and AH_x amorphous gel in the CAC matrix (Fig. 8 a). In the structure of those specimens cured at 200 °C (Fig. 8 b), irregular cubic C_3AH_6 crystals, completely or partially covered by AH_3 crystalline material, are observed. The samples were also contaminated by carbonation and re-hydration due to difficulties in preparations. Considerable changes in structure of CAC matrices were found after heating at 1000 °C (Fig. 7). The contours of the cubic and irregular cube crystals has significantly diminished (remainings are probably due to rehydration of the specimens), replaced by the increased amount of small pores.

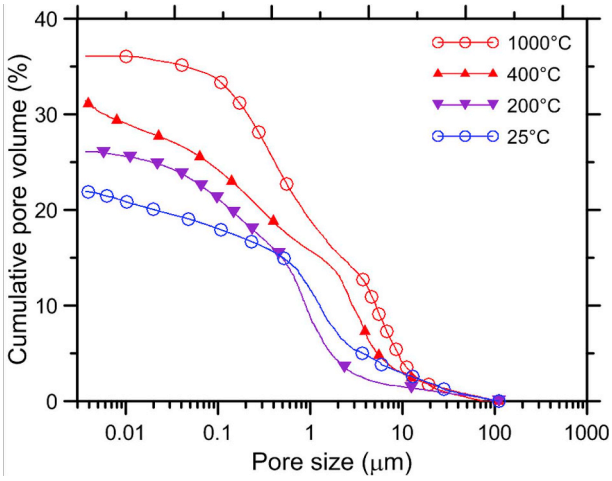

Fig. 7. Cumulative pore size distribution curve (MIP): effect of temperature.

4. Discussion

The proposed model for hydration reactions rests on the following assumptions: a) single reaction scheme eq. (2) for hydration at 25 °C, where AH_3 is used for AH_x gel, justified by difficulty to separate hydration reactions eqs. (2), (5) and (6), and also by drying sensitivity of metastable hydration products; b) single reaction eq. (3) for converted samples at 200 °C; c) the only reactive minerals considered are CA and $C_{12}A_7$; and d) their hydration is congruent, i.e. exhibit same rates, $\alpha_{CA} = \alpha_{C12A7}$ during hydration. The hydration of $C_{12}A_7$ was treated together with CA hydration by simply increasing the CA quantity by the

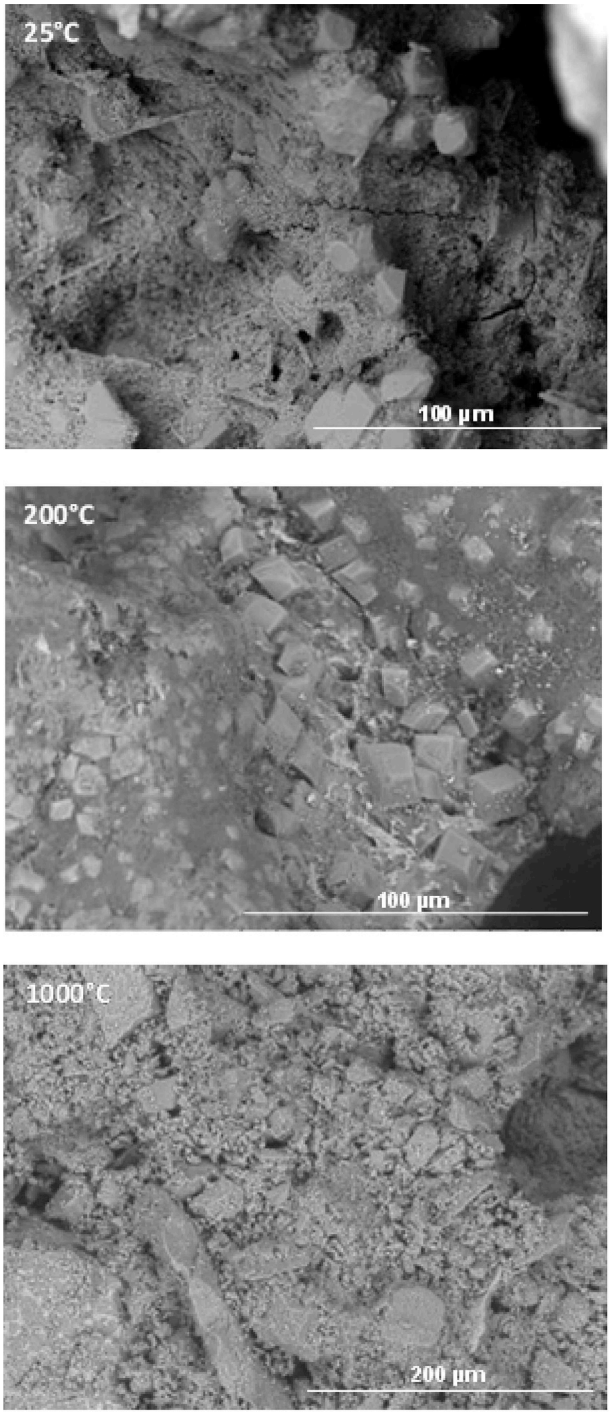

Fig. 8. SEM secondary electron mode images.

amount of $C_{12}A_7$ in CAC. The assumption of their congruent hydration and similar reaction stoichiometry is justified by the small amount of $C_{12}A_7$ in the CAC (4% $C_{12}A_7$ and 60% CA, based on QXRD results). Although there is a relatively high amount of C_2AS (22% in cement and 16% in Alag), no significant amount of C_2ASH_8 was formed. Low reactivity of C_2AS is probably due to low w/c ratio employed and sealed curing conditions. The water available for the hydration is primarily consumed by much faster reactions of CA minerals. In long term hydration, and especially when additional external water is absorbed into material, C_2AS hydration may become significant, and should be then included in the model.

The volume of formed hydration products per 1 g of completely reacted mineral calculated by eq. (18), according to reaction eqs. (1)–(3), is 1.243 cm^3/g, 0.780 cm^3/g and 0.586 cm^3/g, respectively. Furthermore, by reference to eq. (16), the $(H/CA)_{tot}$ for the individual CA hydration reaction (1), (2) and (3) is 1.1385, 0.6262 and 0.4557, respectively.

Bound water (*BW*) and released water (*RW,* in vol % of paste obtained as a difference between the total 'mixed' water and the bound water) for the CAC mortars plotted in Fig. 10 as a function of temperature show good agreement between model and experimental results. Good agreement can be also observed, Fig. 11, between predicted and measured (obtained from solid density) paste porosities. Fig. 11 plots also the MIP porosities normalized to cement pastes, which are obtained by subtracting the 14 vol % of air bubbles from the mortar MIP porosities (Table 6), and then dividing by the volume fraction of paste (0.4551, calculated from cement and water amount from Table 2) in the mortar, i.e. $P_{paste} = (P_{mortar} - 14)/0.4551$. The air content of 14% is calculated from the measured apparent density of the mortar specimens. One can observe, on Fig. 11, that MIP paste porosities are always significantly lower than the ones obtained from the measured densities of solid mortar powders. This can be attributed to the distribution of air bubbles in the specimens, which is not ideally homogenous. Relatively small samples (2 cm^3) for MIP analysis, taken from the center of the specimen, thus may not be fully representative as they may contain different amounts of air bubbles than the rest of the specimen. It can be expected that more air bubbles are located more at the top of the specimen than at the bottom, due to segregation effects. However, considering the small w/c and addition of viscosity modifying agent for improving the cohesion of fresh mortar that avoids segregation of the components, a relatively good stability of the air bubbles is expected.

Higher discrepancy at 400 °C, for *BW*, *RW* (Fig. 10) and porosity (from solid density, Fig. 11), can be explained by incomplete decomposition of the stable hydration products (addressed further in the last paragraph) and/or carbonation processes during heating of the specimens, which results in a higher amount of *BW*, accompanied by lower amount of released water and porosity, in the measured values rather than in the predicted ones.

Predicted values for both 400 °C and 1000 °C samples are the same as they both assume (as a first simplification) that a complete dehydration process has occurred: $BW_{model} = 0$ g/g CAC, porosity and $RW = 51.5\%$. Predicted amounts of released water (*RW*) is 7.3% and 15.7%, for 25 °C and 200 °C samples, respectively, while the predicted bound water is 0.3006 g/g CAC and 0.2432 g/g (Fig. 10), and predicted porosity is 20.1% and 31.8% (Fig. 11).

CA hydration reactivity, Fig. 11 - right ordinate, increases up to 400 °C due to initial hydration reactions taking place at 25 °C which is then further stimulated by conversion reactions taking place during heating to 200 and 400 °C. A higher degree of reacted CA at 400 rather than at 200 °C could be attributed to a higher reaction temperatures under wet, i.e. hydro-thermal conditions assured by a slow transport of moisture within the specimen that gradually reaches the drying-out equilibrium with respect to the evaporated water content. At 1000 °C the degree of reacted CA is significantly lower, which can be explained by crystallization of CA around 1000 °C [35], also corroborated by an exothermal peak observed in the DSC curve around 990 °C (not shown here). Evolution of $C_{12}A_7$ mass fraction in anhydrous mortar as a function of temperature is presented in Fig. 12. Initial $C_{12}A_7$ reactivity at 25 °C was negligible, but this measurement was quite insensitive because of very small amounts of $C_{12}A_7$ in cement (4%) compared to larger amounts of it (11%) in higher proportion of Alag aggregates in mortar. The reactivity of Alag is expected to be low, as the reactive surface area of the coarse grains is relatively low. The main amount of $C_{12}A_7$ is thus hidden inside the poly-mineral grains and blocked for reaction by a layer of slow reacting anhydrous minerals. However, semi-quantitative results in Fig. 12 could show a relatively higher reactivity at 200 °C due to transformation reactions, followed by crystallization of $C_{12}A_7$ at 400 and 1000 °C. The amount of crystallized $C_{12}A_7$, already at 400 °C, as well as CA at 1000 °C,

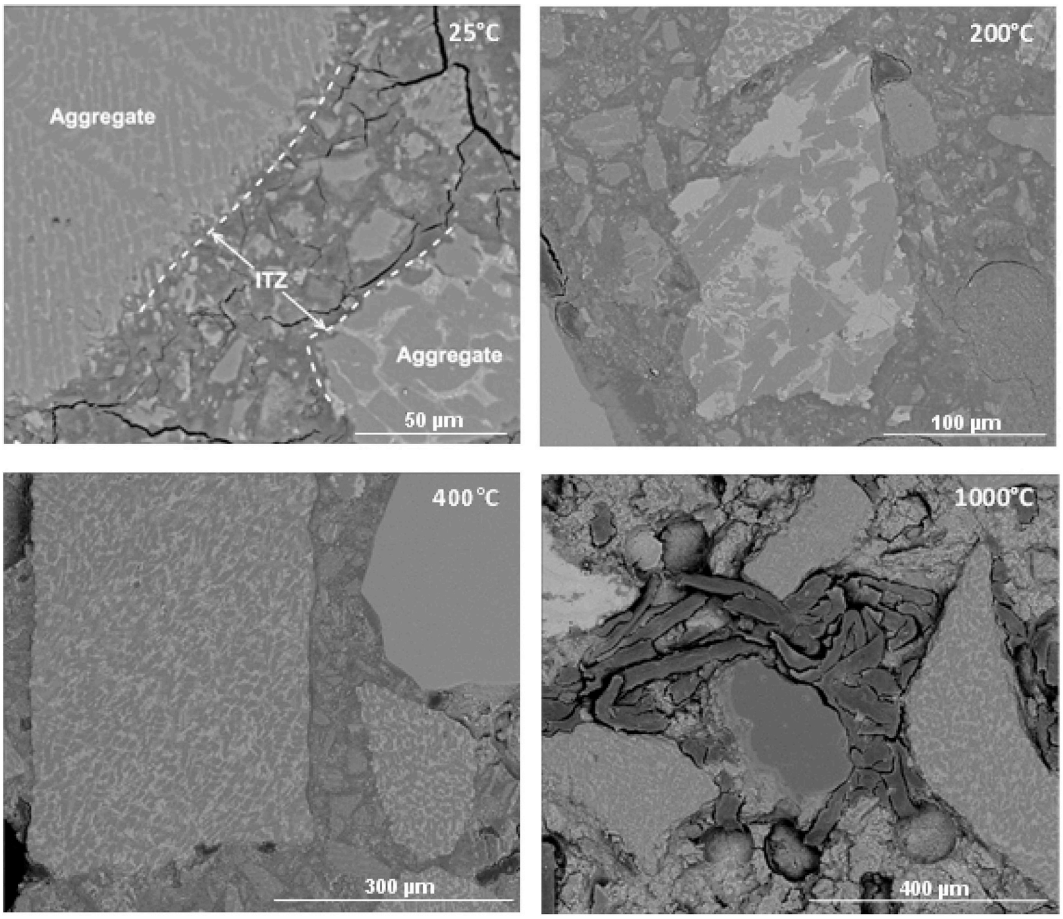

Fig. 9. SEM back scattered electron (*bse*) images of CAC mortar samples at room temperature and after heating process up to 200, 400 and 1000 °C. The *bse* grey scaling depends on the average atomic number , where bright areas represent slow reacting phases containing higher average atomic number compouds: C_4AF, CT, C_2AS.

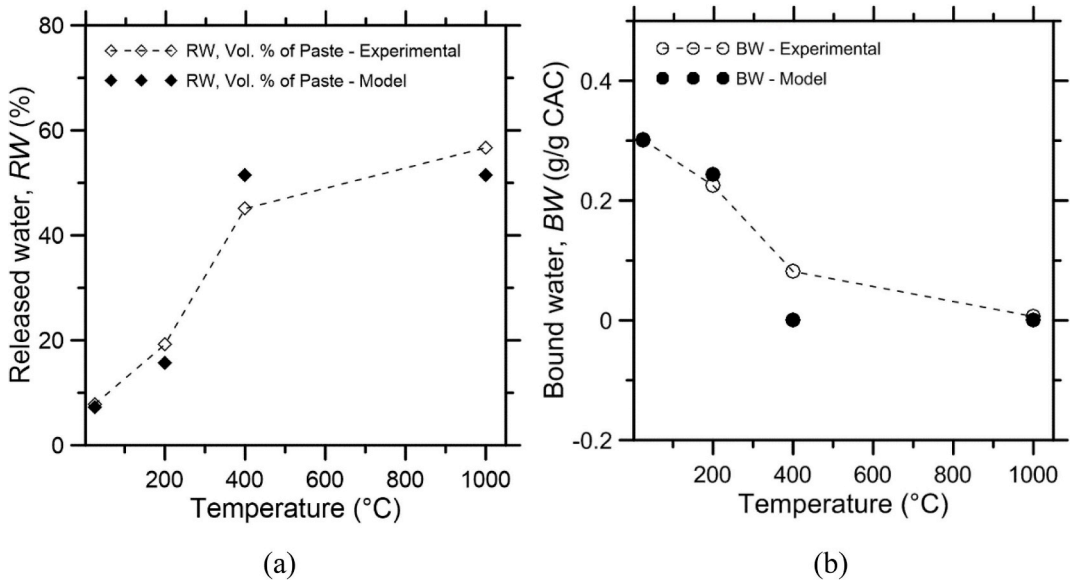

Fig. 10. Released water (*RW,* vol % of paste, calculated as a difference between total 'mixed' water and bound water) (a) and bound water (*BW*) (b) for CAC mortars as a function of temperature: comparison of model and experimental values.

at such relatively low temperatures [17] can be ascribed to a high degree of homogenisation (intermixing) of amorphous dehydrated precursors according to their stoichiometric mass ratios, which is discussed later with eqs. (21) and (22).

The w/c and the amount of main active minerals in CAC are the principal variables governing the porosity and strength development during the transformation reactions [1]. This is because the free water is released by transformation reactions (eqs. (4)–(6)), as metastable

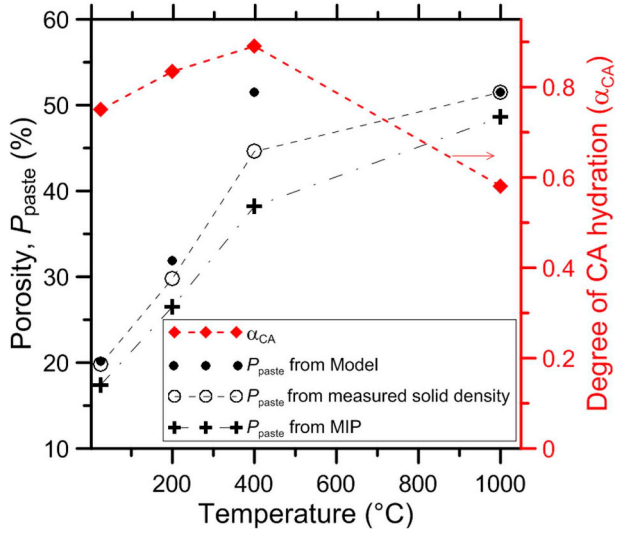

Fig. 11. Evolution of porosity obtained from measured mortar solids density (Table 6) and eqs. (11), (12) and (14) and mortar MIP results (Table 6): comparison of model and experimental porosity normalized to paste volume without air bubbles. Right ordinate shows CA hydration reactivity up to 400 °C, and re-crystallization reactivity at 1000 °C. Degree of reacted CA was obtained from XRD measurements and eq. (9) and was used as input for modeling predictions.

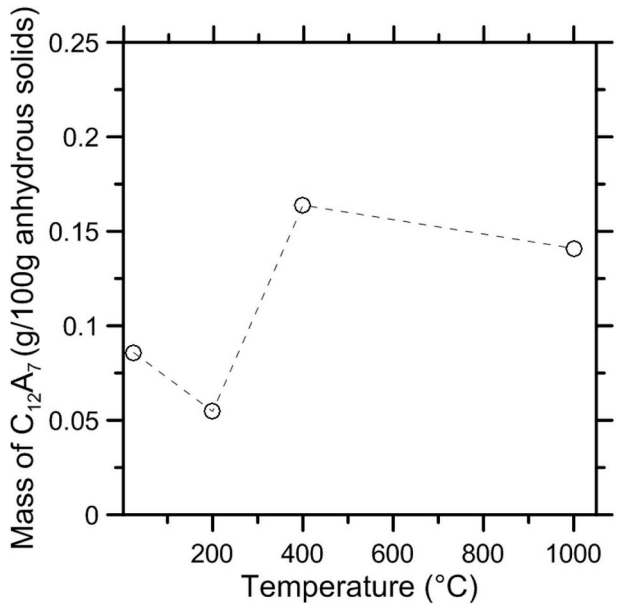

Fig. 12. Evolution of $C_{12}A_7$ mass fraction as a function of temperature, results are normalized to anhydrous solids, i.e. mass of fired (at 1000 °C) mixture of cement and aggregates.

hydration products contain more structural water than stable ones, which contributes to a further hydration of non-hydrated cement that further fills the porosity. Thus, the deleterious effect transformation reactions have on the properties of CAC-based materials could be reduced by lowering the w/c ratio. Recently this improvement in material properties was demonstrated by usage of a PCE superplasticiser [5]. That study demonstrated that lowering the w/c ratio from 0.470 to 0.291, by superplasticiser addition while fixing the workability, compressive strengths were improved up to 41% for mortars with mainly metastable hydration products and by up to 90% for the specimens with transformed hydration products. Conversion of CAH_{10} and C_2AH_8 to C_3AH_6 theoretically results in 75% and 47% volume reduction, relative to the original volume of hydration products, normally leading to strength retrogression. For our mortar systems, with clinker aggregates, the predicted increase in paste porosity is 58%, i.e. from 20.1% to 31.8% (Fig. 11). Although the converted strength of conventional CAC-based materials (without clinker aggregates) is lower than the initial metastable strength, in relative terms, the converted strength is greater than metastable one at comparative higher w/c ratios [5]. This could be attributed to the fact that C_3AH_6 and gibbsite are expected to be stronger than metastable (amorphous and layered [14]) hydration products, which results in stronger bonding [1]. However, in conventional CAC-based materials the adverse effect of an increase in porosity prevails over a better bonding of stable hydration products.

Without reactive clinker aggregates, the transformation process is generally documented to impair compressive strength, in reference with the maximal metastable one, indicating that the increase of material porosity prevails the effect of further increase in degree of hydration. Moreover, the stable hydration products contain more crystalline OH^- bonds, and a higher crystalline level. The stable hydration products have a much lower capacity for filling the capillary porosity in CAC paste than the metastable ones. This results in lower porosity (and hence provisionally better performances) for metastable phase although the hydration degree is lower. Chemically bound water for complete hydration of considered active minerals (in this paper CA and $C_{12}A_7$ in the investigated cement), the $(H/CAC)_{tot}$ upon reaction eqs. (1)–(3) is calculated by (H/CA w_{CA}), where the CA content is increased by the $C_{12}A_7$ content, to be 0.73 g/g CAC, 0.40 g/g CAC and 0.30 g/g CAC, respectively.

The poly-mineral nature of aggregate grains results in selective dissolution of its surface leaving the slow reactive iron-containing minerals (brighter areas in SEM-bse images, Fig. 9) sticking out into the hydration products of the surrounding cement paste's interfacial zone. This enables the mechanical interlocking effect between Alag aggregate and paste. SEM micrographs (Fig. 9) show excellent bonding between aggregates and cement paste, and an even more compact matrix (Fig. 8) for 200 °C than 25 °C. This paper shows that in spite of the increased cement paste porosity from 21% to 32% upon heating the specimens at 200 °C, the induced conversion reactions resulted in improved mechanical properties. This was attributed to a better bonding within the interfacial zone, and by a stronger nature of the stable hydration products, compared to weaker amorphous and layered metastable products (with high amount of loosely held water molecules), which is further stimulated by an increased degree of cement and aggregate hydration that improves the mechanical interlocking effect between Alag aggregate and the paste components.

As no portlandite was observed at 400 °C (nor CaO at 1000 °C), following sintering reaction can describe the crystalisation of $C_{12}A_7$ from a decomposition of C_3AH_6 and AH_3:

$$4C_3AH_6 + 3AH_3 \rightarrow C_{12}A_7 + 33H \quad (21)$$

At 400 °C, $C_{12}A_7$ might also contain some remaining amounts of crystalline water ($C_{12}A_7H$) [28]. The stoichiometry of reactants in this dehydration (and re-crystalisation) reaction, molar ratio of $n(AH_3)/n(C_3AH_6) = 3/4$, consumes less AH_3 than available, as formed according to hydration reaction eq. (3) where $n(AH_3)/n(C_3AH_6) = 2/1$. This may be attributed to the nature of the crystallization process and by the sintering mechanism which occurs preferentially on the boundaries of particles of the dehydrated phases. At 1000 °C, CA crystalizes by sintering reaction of $C_{12}A_7$ with amorphous A:

$$C_{12}A_7 + 5A \rightarrow 12CA \quad (22)$$

Both these crystallization processes are formed by sintering reactions where atoms in the material's microstructure diffuse across the boundaries of the particles, fusing the particles together and creating a new solid phase. Therefore, an observed low degree of conversion for these reactions can be explained by their strongly kinetically (diffusion)

controlled mechanism. From this, the reaction initially takes place only at boundaries where the two reacting phases meet, i.e. amorphous C_3A, formed by dehydration of C_3AH_6, and amorphous A, from AH_3 dehydration. A better intermixing of these two phases, as a result of (through solution [23]) hydration precipitation reactions, leads to higher reactive surface areas and thus also the higher sintering reaction rate [31]. The dehydration products react to produce new crystalline phases, which create a load bearing capacity via ceramic bonds (Fig. 9), largely due to intergrowth of newly crystalized $C_{12}A_7$ and/or CA crystals with the aggregates. At 400 °C gibbsite loses part of its crystalline water, and transforms to boehmite (gamma-AlOOH)) [29]. The XRD patterns of gibbsite after heating at 400 °C indicate a trace of boehmite (at 14.5° 2θ CuK_{alpha}) along with the disappearance of gibbsite peaks. Boehmite then further decomposes to amorphous aluminum oxide and semi-crystalline χ-Al_2O_3 [29]. At 400 °C and 1000 °C, traces of χ-Al_2O_3 phase could be detected (Fig. 6 b), which gradually loses water until about 800 °C [29,30]. Therefore, for the 400 °C samples, the TG loss (Fig. 5) and the model-measurement discrepancy (Fig. 10) can be attributed, beside carbonation, also to remaining water in $C_{12}A_7H$ [28] and AlOOH [29,30].

5. Conclusions

Including reactive Alag aggregates into mortars with a low w/c ratio, was found to increase the strength by 7% and 12% at room temperature curing for 14 and 28 days, respectively, in comparison to the CAC matrix with 7 days of age. The CAC mortar specimens heated up to 200 °C showed a substantial increase in compressive strength of 24%, followed by a decrease of 22% and 57%, for 400 °C and 1000 °C, respectively. The same trend was reflected in the elastic modulus: increase in the elastic modulus of 8% at 200 °C, and a decrease of 58% and 70% at 400 °C and 1000 °C, respectively.

The results show that in spite of the increasing porosity of the cement paste from 21% to 32% upon heating the specimens at 200 °C, the induced conversion reactions resulted in improved mechanical properties. This may be attributed to 1) a better bonding within the interfacial zone by stronger stable hydration products, compared to the weaker metastable products, and 2) an increased degree of aggregate and cement hydration reaction which improves the mechanical interlocking effect between Alag aggregates and paste. The poly-mineral nature of the aggregate grains results in a selective dissolution of its surface leaving the slow reactive iron-containing cement minerals sticking out into the hydration products of the surrounding cement paste interfacial zone, contributing also to a reinforced bond.

CA hydration reactivity increases up to 400 °C, explained by a lower initial hydration reactions (at 25 °C) which is further stimulated by conversion reactions taking place during heating to 200 and 400 °C. At 1000 °C the degree of reacted CA is significantly lower, which can be explained by crystallization of CA around 1000 °C. A certain amount of $C_{12}A_7$ shows reactivity due to conversion reactions at 200 °C, followed by crystallization of $C_{12}A_7$ at 400 and 1000 °C.

The effect of temperature increase on cumulative pore-size distribution shows an increase in pore size at 400 and 1000 °C attributed to the decomposition of hydration products. The metastable material at 25 °C exhibits a tendency towards larger pores than converted samples (200 °C).

Model predictions, based on the main chemical reaction for CA minerals fit fairly well the experimental results for both chemically-bonded and evaporated water, as well as for porosity, as a function of the temperature. The discrepancy at 400 °C may be attributed to carbonation and persisting crystalline water in $C_{12}A_7H$ and AlOOH.

Acknowledgements

This research was supported by the Brazilian Agency CNPq (grant number: 141937/2012-2) and TU Darmstadt. We thank Kerneos (France) for supplying the cement, superplasticizer and aggregate. We thank our colleague Dr. Reiner Neumann (CETEM - Centro de Tecnologia Mineral, Rio de Janeiro, Brazil) for his invaluable contribution to QXRD measurements. Finally, the support to networking activities provided by the SUPERCONCRETE Project (H2020-MSCA-RISE-2014 n 645704; http://www.superconcreteh2020.unisa.it/) funded by the European Union is gratefully acknowledged.

References

[1] J. Bensted, J. Bensted, P. Barnes (Eds.), Calcium Aluminate Cements, Chapter 4 in Structure and Performance of Cements, 2end ed., 2002 0-419-23330-X, pp. 114–138 London.
[2] R.J. Mangabhai, F.P. Glasser (Eds.), Proc. Int. Conf. On CAC, Edinburgh, UK, 2001 1-86125-142-4.
[3] Calcium aluminates, in: C.H. Fentiman, R.J. Mangabhai, K.L. Scrivener (Eds.), Proceedings of the International Conference 2014, IHS BRE Press, Avignon, France, 978-1-84806-316-7, May 2014, pp. 18–21.
[4] C.M. George, P. Barnes (Ed.), Industrial Aluminous Cements in Structure and Performance of Cements, Applied Science, London, 1983, pp. 415–470.
[5] K.L. Scrivener, J.L. Cabiron, R. Letourneux, High-performance concretes from calcium aluminate cements, Cement Concr. Res. 29 (1999) 1215–1223, https://doi.org/10.1016/S0008-8846(99)00103-9.
[6] C. Wöhrmeyer, C. Alt, N. Kreuels, C. Parr, M. Vialle, Calcium Aluminate Aggregates for Use in Refractory Castables, TP-GB-RE-LAF-016, (1998), pp. 1–13 http://www.secar.net/-Technical-Papers.
[7] C. Wöhrmeyer, C. Parr, H. Fryda, E. Frier, New Calcium Aluminate Aggregates for Refractory Castables Installed in Highly Abrasive Environments, TP-GB-RE-LAF-092, (2011), pp. 1–13 http://www.secar.net/-Technical-Papers.
[8] C. Wöhrmeyer, C. Parr, H. Fryda, E. Frier, Aggregates for Non-ferrous Applications, Kerneous, TP-GB-LAF-094, (2011), pp. 1–12 http://www.secar.net/-Technical-Papers.
[9] Calcium aluminate cements, in: C.H. Fentiman, R.J. Mangabhai, K.L. Scrivener (Eds.), Proceedings of the Centenary Conference, IHS BRE Press, 978-1-84806-045-6, 2008.
[10] A.M. Goyns, M.G. Alexander, Performance of various concretes in the Virginia experimental sewer over 20 years, Calcium Aluminates. Proceedings of the International Conference 2014, Avignon, France, 18–21, May 2014, pp. 573–584.
[11] J. Herisson, E.D. Van Hullebusch, M. Guéguen-minerbe, T. Chaussadent, Biogenic corrosion mechanism: study of parameters explaining calcium aluminate cement durability, Calcium Aluminates. Proceedings of the International Conference, 2014, pp. 633–644. Avignon, France, 18–21 May 2014.
[12] M.L. Berndt, Protection of concrete in cooling towers from microbiologically influenced corrosion, Trans. Geoth. Resour. Counc. 25 (2001) 3–7.
[13] S. Lamberet, D. Guinot, E. Lempereur, J. Talley, C. Alt, Field investigations of high performance calcium aluminate mortar for wastewater applications, Calcium Aluminate Cements: Proceedings of the Centenary Conference, IHS BRE Press, Avignon, 978-1-84806-045-6, 2008, pp. 269–277.
[14] D.V. Heerden. The use of calcium aluminate cement in shotcrete. In: Shotcrete: More Engineering Developments: Proceedings of the Second International Conference on Engineering Developments in Shotcrete, Bernard (ed), October 2004, Cairns, Queensland, Australia.
[15] C. Wöhrmeyer, C. Parr, H. Fryda, E. Frier, New Stronger Bonds for Monolithic Castables through Surface Reactive Calcium Aluminate Aggregates, TP-GB-RE-LAF-085, (2010), pp. 1–9 http://www.secar.net/-Technical-Papers.
[16] C. Gosselin, E. Gallucci, K. Scrivener, Influence of self heating and Li2SO4 addition on the microstructural development of calcium aluminate cement, Cement Concr. Res. 40 (2010) 1555–1570, https://doi.org/10.1016/j.cemconres.2010.06.012.
[17] N. Ukrainczyk, Effect of Polycarboxylate superplasticizer on properties of Calcium aluminate cement mortar, Adv. Cem. Res. 27 (7) (2015) 388–398 https://doi.org/10.1680/adcr.14.00022.
[18] W.E. Lee, W. Vieira, S. Zhang, K.G. Ahari, H. Sarpoolaky, C. Parr, Castable refractory concretes, Int. Mater. Rev. 46 (2001) 145–167, https://doi.org/10.1179/095066001101528439.
[19] C. Gogtas, H.F. Lopez, K. Sobolev, Role of cement content on the properties of self-flowing Al2O3 refractory castables, J. Eur. Ceram. Soc. 34 (2014) 1365–1373, https://doi.org/10.1016/j.jeurceramsoc.2013.11.004.
[20] N. Ukrainczyk, Chemical shrinkage during hydration reactions of calcium aluminate cement, Austin J. Chem. Eng. 1 (2014) 1–7.
[21] Abnt, NBR NM 248: Agregados - Determinação da composição granulométrica, Test, (2003), p. 6.
[22] F. De Larrard, Concrete Mixture Proportioning: a Scientific Approach. London. E& FN SPON, (1999).
[23] T. Sedran, Rhéologie et rhéométrie des bétons: application aux bétons autonivelants, Doctoral dissertation Ecole Nationale des Ponts et Chaussées, 1999, p. 484.
[24] J.C. Taylor, L.P. Aldridge, C.E. Matulis, I. Hinczak, Chapter 18 X-ray powder diffraction analysis of cements, in: J. Bensted, P. Barnes (Eds.), Structure and Performance of Cements, 2end ed., 2002 0-419-23330-X, pp. 420–442 London.
[25] F. Chung, Quantitative interpretation of X-ray diffraction patterns of mixtures. II. Adiabatic principle of X-ray diffraction analysis of mixtures, J. Appl. Crystallogr. 7 (1974) 526–531, https://doi.org/10.1107/S0021889874010387.
[26] H.G. Midgley, Quantitative determination of phases in high alumina cement

clinkers by X-ray diffraction, Cement Concr. Res. 6 (1976) 217–223, https://doi.org/10.1016/0008-8846(76)90119-8.
[27] N. Ukrainczyk, Kinetic modeling of calcium aluminate cement hydration, Chem. Eng. Sci. 65 (2010) 5605–5614, https://doi.org/10.1016/j.ces.2010.08.012.
[28] R.N. Edmonds, A.J. Majumdar, The hydration of 12CaO.7A12O3 at different temperatures, Cement Concr. Res. 18 (1988) 473–478, https://doi.org/10.1016/0008-8846(88)90082-8.
[29] K.L. Scrivener, A. Capmas, 13 - calcium aluminate cements, Lea's Chem. Cem. Concr. fourth ed., 2003, pp. 713–782 https://doi.org/10.1016/B978-075066256-7/50025-4.
[30] F.M. Lea, The Chemistry of Cement and Concrete, third ed., Edward Arnold, London, 0-7131-2277-3, 1976.
[31] N. Ukrainczyk, T. Matusinovic, S. Kurajica, B. Zimmermann, J. Sipusic, Dehydration of a layered double hydroxide-C_2AH_8, Thermochim. Acta 464 (2007) 7–15, https://doi.org/10.1016/j.tca.2007.07.022.
[32] M.C. Ball, The thermal dehydroxylation of C_3AH_6, Cement Concr. Res. 6 (1976) 419–420, https://doi.org/10.1016/0008-8846(76)90107-1.
[33] A. Malki, Z. Mekhalif, S. Detriche, G. Fonder, A. Boumaza, A. Djelloul, Calcination products of gibbsite studied by X-ray diffraction, XPS and solid-state NMR, J. Solid State Chem. 215 (2014) 8–15, https://doi.org/10.1016/j.jssc.2014.03.019.
[34] B. Zhu, B. Fang, X. Li, Dehydration reactions and kinetic parameters of gibbsite, Ceram. Int. 36 (2010) 2493–2498, https://doi.org/10.1016/j.ceramint.2010.07.007.
[35] A.A. Goktas, M.C. Weinberg, Preparation and crystallization of sol-gel calcia-alumina compositions, J. Am. Ceram. Soc. 74 (1991) 1066–1070, https://doi.org/10.1111/j.1151-2916.1991.tb04344.x.